Journal of Fluids and Structures 18 (2003) 103–118

JOURNAL OF FLUIDS AND STRUCTURES

www.elsevier.nl/locate/jnlabr/yjfls

Hysteresis phenomenon in the galloping oscillation of a square cylinder

S.C. Luo*, Y.T. Chew, Y.T. Ng

Department of Mechanical Engineering, National University of Singapore, 10 Kent Ridge Crescent, Singapore 117576, Singapore

Received 3 August 2002; accepted 30 June 2003

Abstract

It is well known that a square cylinder with one side normal to a uniform stream will gallop when a critical flow velocity is exceeded. It is also quite well known that there is a hysteresis phenomenon in the variation of the cylinder's galloping amplitude with the flow velocity. However, little is known about the cause of this hysteresis phenomenon, and the objective of this paper is to study it more closely. In the present study, flow over a stationary square cylinder at different angle of attack (α) and at Reynolds number (Re) of 250 and 1000 was investigated numerically by using a 2-D hybrid vortex computation scheme. The study reveals that the well known point of inflection which exists in the side force (C_y) versus α plots at high Reynolds number only occurs at $\mathrm{Re}=1000$, $\alpha=4^\circ$ in the present numerical simulation. Nonlinear analysis further reveals that this point of inflection is the cause of the hysteresis phenomenon. By further analysing the computed flow field, it is noted that at $\mathrm{Re}=1000$, $\alpha=4^\circ$, intermittent flow reattachment takes place at alternate vortex shedding cycle on one side of the cylinder. This results in larger side force fluctuation, and it is conjectured that such large side force fluctuation affects the increasing trend of the side force with angle of attack, resulting in the point of inflection reported earlier. The above-mentioned alternate cycle flow reattachment was much less prominent at $\alpha=2^\circ$ and 6° ($\mathrm{Re}=1000$), and was not observed at $\mathrm{Re}=250$. Finally, dye flow visualization was carried out in a recirculating water tunnel and the results at $\mathrm{Re}=1000$ confirms the existence of the intermittent flow reattachment. However, in the experiment, flow reattachment does not take place in a very regular alternate cycle manner as in the computation. Instead, it occurs intermittently, possibly due to three-dimensional effects in real flow.

1. Introduction

The aeroelastic behaviour of a bluff cylinder, including the galloping response of a square cylinder, has been studied extensively in the past few decades. Galloping vibration represents a classical instability mechanism in the flow over a square cylinder. Through the works of many researchers, which include Parkinson and Brooks (1961), Parkinson and Smith (1964), Bearman et al. (1987), Bearman and Luo (1988) and Belvins (1990), much light has been shed on this instability mode. Of great interest is the hysteresis phenomenon in the variation of the cylinder's galloping amplitude with the flow velocity. This phenomenon occurs within a certain speed range and depending on whether the reduced velocity is increasing or decreasing, the vibration amplitude can assume a lower or higher value, respectively.

In the classic papers by first Parkinson and Brooks (1961) and later Parkinson and Smith (1964), the quasi-steady theory was proposed. This theory assumes that the aerodynamic forces experienced by an oscillating square cylinder at any instant in time is equivalent to that exerting on a static cylinder, placed at different angles of incidence. The reason

*Corresponding author. Tel.: +65-876-2265; fax: +65-779-1459.
E-mail address: mpeluosc@nus.edu.sg (S.C. Luo).

0889-9746/$ - see front matter
doi:10.1016/S0889-9746(03)00084-7

being in the former, the relative air-flow appears to be approaching the vibrating cylinder at varying angle of attack. Hence, a polynomial curve fit onto the side force coefficient C_y versus α data represents the unsteady aerodynamic forces acting on a galloping square cylinder, and the polynomial coefficients from the fitted curve act as inputs to the equation of motion. The work of Parkinson and Smith (1964) was an improvement over that of Parkinson and Brooks (1961), in that the former used a seventh order polynomial (instead of a fifth order polynomial) to describe the C_y versus α relation. With the seventh order polynomial, the point of inflection in the C_y versus α curve can be represented fairly accurately and the hysteresis phenomenon is present in the subsequent amplitude of oscillation ($\bar{Y}$) versus reduced velocity (U) relation. Hysteresis was previously not observed by Parkinson and Brooks (1961) when they modelled the C_y versus α relation with a fifth order polynomial. The above led one to question whether the point of inflection in the C_y versus α plot is related to the hysteresis phenomenon seen in the amplitude versus reduced velocity graph.

Other researchers, such as Norberg (1993), contributed to the quasi-steady theory by using the static cylinder method in his work. Norberg (1993) found, experimentally, that the hysteresis region in the amplitude-reduced velocity plot is Reynolds number dependent. Bearman et al. (1987) and Bearman and Luo (1988) tested the validity of the quasi-steady theory by using different damping levels and reduced velocity. This area of work is important because bluff cylinders are susceptible to both galloping and vortex-induced vibrations, and complex interaction between them can occur. Bearman et al. (1987) concluded that for the quasi-steady theory of galloping to be valid, the critical reduced velocity (reduced velocity at which galloping oscillation commences) must be at least four times the reduced velocity for vortex resonance (U_r). Parkinson and Wawzonek (1981) also performed investigation on the complex interaction between vortex resonance and galloping.

It is apparent that the cause of the hysteresis phenomenon, which is present in the galloping response of a square cylinder, has not been given much attention to date. In the present paper, we will attempt to explain the cause of the hysteresis phenomenon by first establishing a link between the existence of an inflection point in the side force versus angle of attack (C_y versus α) plot and the presence of this hysteresis region by using the quasi-steady theory. We will then attempt to explain the cause of the point of inflection in the C_y versus α relation by using both CFD and experimental (water channel) flow visualization.

2. Numerical method

2.1. Basic equation

A hybrid vortex method developed by Cheng et al. (1997) was used to simulate viscous, incompressible flow over a two-dimensional square cylinder at various angles of incidence. The Reynolds number in the present study is 250 and 1000 and the angle of incidence is from 0° to 45°. The present numerical scheme is based on a combination of the diffusion-vortex method and the vortex in cell method by dividing the flow field into two regions. In the region near the body surface where viscous effects are predominant, a combination of the diffusion-vortex method and vortex-in-cell method are used to solve the Navier–Stokes equation, while the vortex-in-cell method alone is used in the exterior domain where viscous effects are less important. Fig. 1 shows the two regions in the flow domain. For brevity, the details of the numerical method will not be described here (interested readers should refer to Cheng et al. (1997) instead) but the basic steps and governing equations are given as follows:

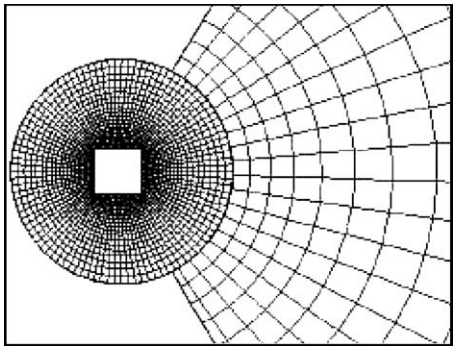

Fig. 1. The computational flow domain is divided into two regions as shown.

For 2-D flow, the stream function-vorticity formulation gives the vorticity transport equation

$$\frac{\partial\zeta}{\partial t}+u\frac{\partial\zeta}{\partial x}+v\frac{\partial\zeta}{\partial y}=\frac{2}{\mathrm{Re}}\left(\frac{\partial^2\zeta}{\partial x^2}+\frac{\partial^2\zeta}{\partial y^2}\right) \tag{1}$$

and the Poisson equation for stream function

$$\nabla^2\psi=-\zeta. \tag{2}$$

The vorticity transport equation is represented by two fractional steps: pure diffusion and inviscid convection. These two equations are solved separately. Thus, for each time step, the diffusion equation is

$$\frac{\partial\zeta}{\partial t}=\frac{2}{\mathrm{Re}}\left(\frac{\partial^2\zeta}{\partial x^2}+\frac{\partial^2\zeta}{\partial y^2}\right) \tag{3}$$

and the inviscid vorticity convection equation is

$$\frac{\partial\zeta}{\partial t}=-\left(u\frac{\partial\zeta}{\partial x}+v\frac{\partial\zeta}{\partial y}\right). \tag{4}$$

In the interior zone where viscous effects are predominant, the vorticity produced at the wall is carried away by convection and diffusion. In this region, flow separation occurs, large deformation of streamlines takes place, and both the diffusion equation and the inviscid convection equation are solved. In the exterior domain, the viscous effects are negligible and therefore the flow far away from the cylinder can be approximated as an inviscid flow. Thus it can undergo only convection and deformation according to the inviscid convection equation. Cheng et al. (1997) stated that the temporal integration is a second order accurate scheme.

Grid and time step dependency tests were performed to ascertain that optimal time step and mesh size were used for the computation. Changes in the values of the drag coefficient (C_d), lift coefficient (C_l) and Strouhal number (St) were monitored at $\alpha=0^\circ$ and 15° when different combinations of the time step ($\Delta t=0.01$, 0.005, 0.0025 and 0.00125) and mesh size ($I\times J=201\times101$, 221×126, 251×151 and 501×301) were used. The test revealed that at a constant time step, both C_d and C_l increase initially with mesh density and their values reach asymptotic values at $I\times J=221\times126$. Beyond that mesh size (at 251×151 and 501×301) there were no significant changes in the magnitudes of C_d and C_l, but the computation time becomes longer. Subsequent comparison of the results computed using the 221×126 mesh and $\Delta t=0.0025$ with those reported by Sohankar et al. (1999) was found to be favourable. The present calculation results in C_d of 1.602, 1.977 and 2.027 and St of 0.138, 0.124 and 0.122 at $\mathrm{Re}=250$, 500 and 1000, respectively. The above data were found to fall well within the band of data obtained by Sohankar et al. (1999) and other researchers (Fig. 3 in Sohankar et al., 1999). At $\mathrm{Re}=1000$, the present data were estimated to be within about 1.5% from the data of Sohankar et al. (1999). Hence, all things considered, the combination of a time step of 0.0025 and a mesh size of 221×126 was used to compute all the results shown in subsequent sections.

3. Results and discussion

3.1. Variation of C_y with time at $Re=250$ and 1000

The sign conventions for positive V, α, lift and drag forces are defined in Fig. 2. The drag coefficient (C_d) and lift coefficient (C_l) for the two Reynolds numbers and at different α were computed in this simulation. The side force coefficient (C_y) was calculated for different α for $\mathrm{Re}=250$ and 1000. Of particular interest to the present study are the C_y at $\alpha=2^\circ$, 4° and 6° and they are plotted in Figs. 3 and 4 as the instantaneous variation of C_y against time for $\mathrm{Re}=250$ and 1000, respectively. These data were obtained when the respective vortex shedding processes have stabilized and are free from any starting flow (transient) behaviour. For the case of $\mathrm{Re}=250$ (Fig. 3), when α changes, the variation of C_y with time remains fairly sinusoidal, and the amplitude is relatively small. However, distinctive variation can be seen at $\mathrm{Re}=1000$ (Fig. 4) when the angle of attack changes. At $\alpha=2^\circ$, there is a distinct reduction in the side force amplitude in one out of every three cycles, suggesting the shedding of a weaker vortex in that cycle. At $\alpha=4^\circ$ and 6°, the variations are regular and consist of alternate low (more negative) and high (less negative) C_y. Such phenomena were also detected by Shiau et al. (1999), who observed vortex shedding process with strong periodicity of one and three at low Re flows past a square cylinder. They observed that the variations in lift coefficient (C_l) were periodic and, similar to the present results, and the vortex shedding process is repeated in either every cycle (hereinafter referred to as $1T$ periodic) or every three cycles (hereinafter referred to as $3T$ periodic). Subharmonics were also observed by Davis and Moore (1982) in their C_l versus time variation at $\mathrm{Re}=1000$ and $\alpha=0^\circ$, but these subharmonics are absent at

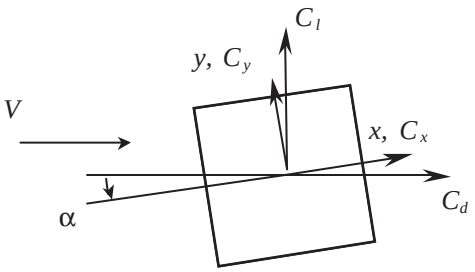

Fig. 2. Sign convention showing the positive directions of the co-ordinates and forces.

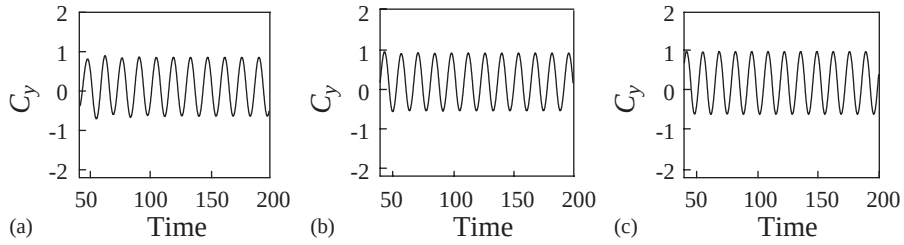

Fig. 3. Instantaneous C_y variation against time for Re = 250 at (a) $\alpha = 2^\circ$, (b) $\alpha = 4^\circ$, and (c) $\alpha = 6^\circ$.

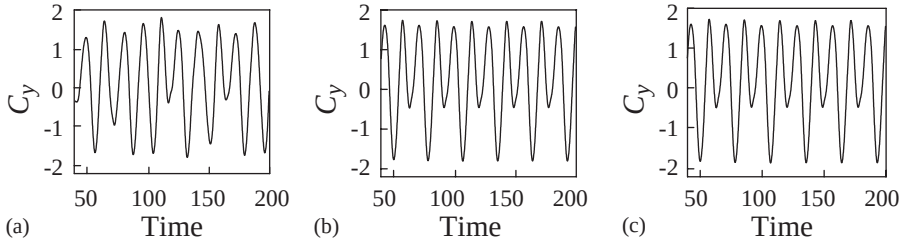

Fig. 4. Instantaneous C_y variation against time for Re = 1000 at (a) $\alpha = 2^\circ$, (b) $\alpha = 4^\circ$, (c) $\alpha = 6^\circ$.

Re = 250. The above signifies the presence of a small low frequency modulation in the shedding frequency at high Re which is absent at Re = 250. The presence of subharmonics seems to be inherent in the vortex shedding process of a square cylinder at higher Re. In the present study, the vortex shedding at Re = 1000, $\alpha = 2^\circ$ appears to be $3T$ periodic (i.e. the flow repeats itself every three cycles of vortex shedding) while those at $\alpha = 4^\circ$ and 6° are $2T$ periodic (the flow repeats itself every two cycles of vortex shedding). By performing a fast-Fourier transform (FFT) on the instantaneous C_y versus time variation at Re = 1000, the subharmonics inherent in the signals are clearly revealed. This is illustrated in Fig. 5, which shows that three spectral peaks are detected for $\alpha = 2^\circ$ (Fig. 5a), while two peaks are detected for $\alpha = 4^\circ$ and 6° (Figs. 5b and c respectively). In the above-mentioned Figs. 5a–c, the dominant frequency is labelled as "1", while the sub-harmonics are labelled as either "2" or "3". It will be shown later, that such C_y versus time variation at 4° is due to the strong upper shear layer reattachment to the side face. This shear layer reattachment occurs in alternate shedding cycles.

The C_y coefficient at various angles of attack is next averaged over many shedding cycles (approximately 60 cycles depending on the different flow cases simulated) to obtain the mean C_y versus α relation at Re = 250 and 1000. The C_y versus α curve for Re = 250 does not show a point of inflection, as illustrated in Fig. 6a; it increases continuously with increasing α until $\alpha = 5^\circ$. At $\alpha = 5^\circ$, C_y begins to decrease, signifying the commencement of shear layer reattachment as discussed in Lee (1975) and Obasaju (1983). At a higher Re of 1000, a point of inflection appears at around $\alpha = 4^\circ$ and this is shown in Fig. 6b. When the angle of attack increases beyond 8°, C_y decreases. The existence of the point of inflection at Re = 1000 is similar to those that occur at higher Reynolds numbers demonstrated in various previous

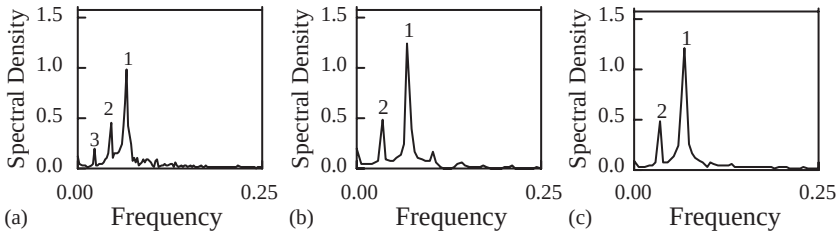

Fig. 5. FFT results showing sub-harmonics in the C_y at Re = 1000 and at (a) $\alpha = 2°$, (b) $\alpha = 4°$, and (c) $\alpha = 6°$. The numbers indicate the dominant shedding frequency (numbered 1) and respective sub-harmonics (numbered 2 or 3).

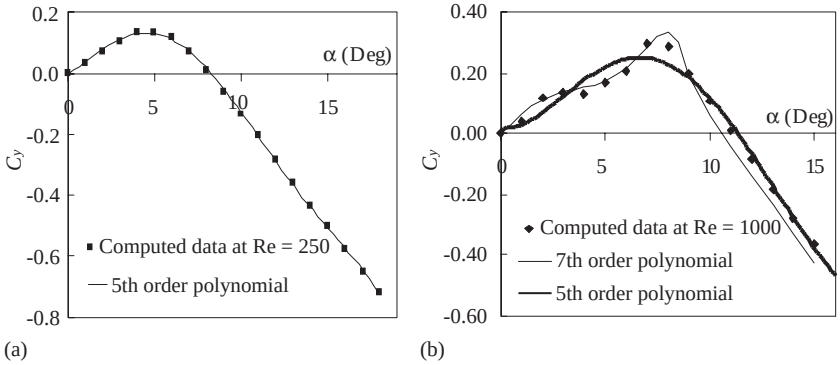

Fig. 6. (a) A fifth order polynomial curve fit onto the C_y versus α data at Re = 250. (b) A fifth and seventh order polynomial curve fit onto the C_y versus α data at Re = 1000.

experimental investigations. However, at Re = 1000, it occurs at a lower angle of attack than those that were reported by Parkinson and Smith (1964), Norberg (1993) and Luo et al. (1994), all at Reynolds numbers higher than 1000.

3.2. Application of quasi-steady theory analysis

The quasi-steady theory proposed by Parkinson and Smith (1964) is adopted in the present study. This theory assumes that a galloping square cylinder operates like a linear elastic system and the equation of motion governing this oscillation is

$$m\ddot{y} + r\dot{y} + ky = \tfrac{1}{2} C_y \rho V^2 hl, \tag{5}$$

where y is the transverse co-ordinate along which the cylinder oscillates, m is the mass, r is the coefficient of viscous damping, k is the spring coefficient of the moving system, C_y is the side force coefficient, ρ and V are the density and velocity of the uniform flow, h and l are the side length and axial length of the square cylinder, respectively. The aerodynamic force coefficient C_y measured on a stationary square cylinder is a function of α and hence also a function of $\dot{y}/V(= \tan\alpha)$. The variation of C_y with α is further approximated by a polynomial in $\dot{y}/V$ over the α range of interest. In Parkinson and Brooks (1961), a fifth order polynomial was used to approximate this C_y versus α relation, while a seventh order polynomial was used in Parkinson and Smith (1964). A higher order polynomial curve fit is required to capture the changes in curvature that arises due to the presence of the point of inflection in the C_y versus α relation. The polynomial approximation can be written as

$$C_y = A\left(\frac{\dot{y}}{V}\right) - B\left(\frac{\dot{y}}{V}\right)^3 + C\left(\frac{\dot{y}}{V}\right)^5 - D\left(\frac{\dot{y}}{V}\right)^7, \tag{6}$$

where A, B, C and D are positive numbers and they are obtained from fitting a polynomial onto the computed data. By substituting Eq. (6) for C_y into Eq. (5), and by averaging the oscillation amplitude over a single cycle, the nondimensional equation used to predict the galloping response is

$$\frac{\mathrm{d}\bar{Y}^2}{\mathrm{d}\tau} = nA\left\{\left(U - \frac{2\beta}{nA}\right)\bar{Y}^2 - \frac{3}{4}\left(\frac{B}{AU}\right)\bar{Y}^4 + \frac{5}{8}\left(\frac{C}{AU^3}\right)\bar{Y}^6 - \frac{35}{64}\left(\frac{D}{AU^5}\right)\bar{Y}^8\right\}. \tag{7}$$

In the above, $\bar{Y}$ is the oscillation amplitude, U is the reduced velocity, β is the reduced damping coefficient, n is defined as the ratio of mass of displaced fluid to twice the mass of the cylinder and τ is the reduce time, ωt, with ω being the natural circular frequency and t as the time. The values of A, B, C and D are the coefficients of the odd power terms in the polynomial curve fit. In the present investigation, both fifth and seventh order polynomial were used to fit the C_y versus α curve for the case of $\mathrm{Re}=1000$, while only a fifth order polynomial was applied to the data at $\mathrm{Re}=250$. Figs. 6a and b show the polynomial curve fitting for the three cases mentioned. A fifth order polynomial is shown to fit the C_y versus α data at $\mathrm{Re}=250$ very well in Fig. 6a, as the data do not contain a point of inflection. However, at $\mathrm{Re}=1000$, the C_y versus α data contain a point of inflection, and Fig. 6b shows that the fifth order polynomial cannot capture it. By using a higher (seventh) order polynomial, the point of inflection was successfully captured.

Through the above exercise, the coefficients of the fifth and seventh order polynomials are obtained and are subsequently used to solve for the stationary oscillation amplitudes (in the way outlined in Parkinson and Smith, 1964) by using Eq. (7). Following their proposed method, the stationary amplitude was solved at different levels of reduced velocity and also at different damping levels, β. In the present investigation, the system is assumed to have the same values of β and n as the system reported in Parkinson and Smith (1964). For the case of $\mathrm{Re}=250$, a fifth order polynomial fit to the C_y versus α data does not result in an inflection point, and the present computation shows no hysteresis behaviour in the amplitude–velocity characteristics (the $\bar{Y}$ versus U relation). Also, a universal curve was obtained when the amplitude and reduced velocity were multiplied by a factor of $nA/2\beta$ and this is illustrated in Fig. 7a. The same procedure was repeated for $\mathrm{Re}=1000$, with the C_y versus α data represented by both fifth and seventh order polynomials. As mentioned earlier, the fifth order polynomial curve fit cannot capture the point of inflection in the C_y versus α data, while the seventh order polynomial can. When the coefficients of the fifth order polynomial were used to solve for the $\bar{Y}$ versus U relation, no hysteresis behaviour is detected. On the other hand, when a seventh order polynomial was used, a hysteresis region can clearly be seen in the $\bar{Y}$ versus U relation. Similar to the $\mathrm{Re}=250$ case, a universal $\bar{Y}$ versus U relation can also be obtained by multiplying the amplitude and reduced velocity with a factor of $nA/2\beta$ and this is shown in Fig. 7b.

To understand more clearly why the point of inflection in the C_y versus α data will result in the hysteresis behaviour in the $\bar{Y}$ versus U relation, we need to look at the problem more closely by using nonlinear stability analysis. In the following, our approach is similar to the one outlined in Parkinson and Smith (1964). By grouping various terms, Eq. (7) is further simplified into the form

$$\frac{\mathrm{d}R}{\mathrm{d}\tau} = aR - bR^2 + cR^3 - dR^4 = F(R), \tag{8}$$

where $R = \bar{Y}^2$. The stationary oscillation amplitude that is attained by the system corresponds to when $\mathrm{d}R/\mathrm{d}\tau = 0$. Hence $R = 0$ (which corresponds to no oscillation) and roots of the equation

$$a - bR + cR^2 - dR^3 = 0 \tag{9}$$

will be the stationary amplitude of oscillation. However, the stability of the stationary amplitude will depend on the gradient of

$$a - bR + cR^2 - dR^3 = F(R). \tag{10}$$

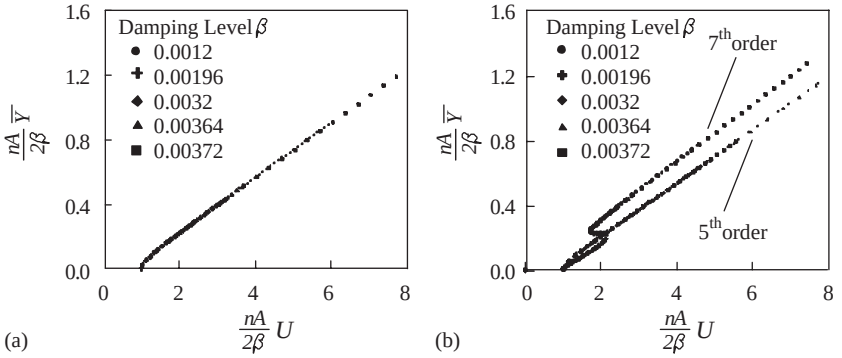

Fig. 7. (a) Universal amplitude versus reduced velocity characteristic for $\mathrm{Re}=250$, using a fifth order polynomial to fit the C_y versus α data. (b) Universal amplitude versus reduced velocity characteristic for $\mathrm{Re}=1000$, using a fifth order polynomial (with no hysteresis region) and a seventh order polynomial (with the presence of a hysteresis region) to fit the C_y versus α data.

That is, a positive gradient indicates unstable roots and hence an unstable oscillation amplitude, and a negative gradient indicates stable oscillation amplitude. When there is no point of inflection in the C_y versus α relation, as demonstrated earlier, a fifth order polynomial is adequate in fitting the C_y versus α data. In this case, Eq. (10) will have the form

$$a - bR + cR^2 = F(R). \tag{11}$$

Solving Eq. (10) for the case at Re = 1000 and Eq. (11) for the case at Re = 250, both stable (S) and unstable (U) roots at various reduced velocity levels can be obtained. For the case of the fifth order polynomial, only one S root was detected at $R = 0$ before the critical reduced velocity of galloping. This shows that the system is stable at zero oscillation amplitude. Beyond the critical reduced velocity of galloping, a U root is detected at $R = 0$ and an S root is detected at a higher R value. This implies that the system is unstable when at rest and will achieve a finite galloping oscillation amplitude. Upon any further increase in reduced velocity, the magnitude of R for the S root increases, but otherwise the results are similar. It is therefore demonstrated here that when there is no point of inflection in the C_y versus α data (fifth order polynomial representation), the system is unstable beyond the critical reduced velocity, and the oscillation amplitude increases with reduced velocity. A one-to-one correspondence exist between $\bar{Y}$ and U.

In contrast, when a seventh order polynomial is used to capture the point of inflection in the C_y versus α curve, additional roots are obtained. Most notably, two S and U roots are found in the hysteresis region and they correspond to the two stationary amplitudes (or two different $\bar{Y}$ values), whereas only one S and one U root are found both before and after this hysteresis region. The collective evidence shows that a hysteresis region can exist when a point of inflection exist in the C_y versus α relation and a seventh order polynomial is used to fit the data.

In the above discussion, by using quasi-steady analysis, we were able to demonstrate that the existence of the point of inflection in the C_y versus α relation leads to the existence of the hysteresis region in the $\bar{Y}$ versus U relation. In the next section, numerical flow visualization and surface pressure distribution data will be used to shed some light on what causes this point of inflection in the C_y versus α relation.

3.3. Numerical flow visualization and surface pressure distribution at Re = 250 and 1000

To supplement the analytical investigation presented above, numerical flow visualization was carried out at $\alpha = 2^\circ$, 4° and 6° for both Re = 250 and 1000. By studying the changes taking place in the flow field, which includes the behaviour of the separated shear layers, we hope to find the reason(s) of why a point of inflection exists in the C_y versus α data at Re = 1000, $\alpha = 4^\circ$. In the following illustrations of Figs. 8–11, vorticity contours for the above-mentioned cases will be shown. In Figs. 8a–c in which the different α cases for Re = 250 are presented, a typical shedding cycle is chosen to illustrate the behaviour of the shear layer. Since the C_y variation for Re = 250 is sinusoidal and highly repeatable, one shedding cycle is sufficient for each of the illustrations. On the other hand, for Re = 1000 at $\alpha = 2^\circ$, 4° and 6°, because of the $2T$ and $3T$ periodic nature of the vortex shedding process, two or three consecutive cycles of shedding must be included in each illustration. Within each series of two or three cycles, the cycles are further divided into strong/weak reattaching cycles and nonreattaching cycles. For example, in Fig. 9 which shows the case of Re = 1000 and $\alpha = 2^\circ$, its vortex shedding is $3T$ periodic and a typical series of shedding cycles consists of two minimum (most negative) C_y values followed by a less negative C_y minimum. Hence, this typical shedding cycle series is subdivided into a nonreattaching cycle and a weak reattachment cycle (points 1–5 and points 5–9 respectively, with points 5 and 9 corresponding to the first two minima) and one strong reattachment cycle (points 9–13, with point 13 corresponding to the third (less negative) minimum).

Similarly, for the case of Re = 1000 and $\alpha = 4^\circ$ (Fig. 10) which is $2T$ periodic, the vortex shedding cycle series is subdivided into a nonreattaching cycle (points 1–5) and a strong reattaching cycle (points 5–9). The same applies to Re = 1000 and $\alpha = 6^\circ$ (Fig. 11) as it is also $2T$ periodic; its typical cycle is divided into a nonreattaching vortex shedding cycle (points 1–5) and a weak-reattaching cycle (points 5–9). The strong, weak and nonreattaching cycles stated here refer to the relative extent of pressure recovery when the upper shear layer reattaches onto the side face. The extent of pressure recovery can be seen in the surface pressure distribution plots illustrated later in Figs. 12 and 13. This way of subdividing the vortex shedding cycle aids in the analysis at a later stage.

By collectively looking at the vorticity plots of Figs. 8a–c, it is noted that at Re = 250, the shear layer reattachment does not take place at $\alpha = 2^\circ$ and 4° (Fig. 8a and b). The upper shear layer does not reattach onto the rear corner and it is more stable throughout the vortex shedding cycle. At $\alpha = 6^\circ$, shear layer reattachment at the upper rear corner is seen and this is shown in Fig. 8c (especially the vorticity contours for points 1 and 5). Beyond $\alpha = 6^\circ$, the mean C_y starts to decrease, and this is related to the continued reattachment of the shear layer onto the side face.

In contrast to the case of Re = 250, the flow structure at Re = 1000 has different features. In the present investigation, intermittent reattachment of the upper shear layer onto the upper side of the cylinder is observed at $\alpha = 2^\circ$, 4° and 6°. To illustrate this shear layer reattachment at different α, a series of vorticity plots for these angles of attack are shown in

Figs. 9–11. These vorticity plots are taken from a typical series of vortex shedding cycles for Re = 1000. Depending on whether the flow is $2T$ or $3T$ periodic, these series of cycles can be two (for $2T$ periodic) or three (for $3T$ periodic) consecutive cycles of vortex shedding. Within each series, the cycles can be further divided into the reattaching or nonreattaching cycles.

To have a better appreciation of the flow configuration, the C_y versus time variation for Re = 1000, at $\alpha = 2^\circ$, 4° and 6° are also included in the vorticity contours plot in Figs. 9–11, respectively. For the case of Re = 1000 and $\alpha = 2^\circ$ (Fig. 9), at point 3 which corresponds to the instant when C_y is at a maximum, the vorticity plot suggests that the upper shear layer does not reattach onto the side face. However, one shedding cycle later, at point 7, a weak shear layer reattachment can be seen; and at yet another cycle later, at point 11, a fairly strong reattachment with the shed vortex close to the rear face is observed. Hence, for the present case the shear layer interacts with the upper rear corner of the cylinder with a combination of no reattachment, weak and strong reattachments that occurs in a $3T$ periodic manner. Similar trends can be seen at $\alpha = 4^\circ$ (Fig. 10) and $\alpha = 6^\circ$ (Fig. 11), but the strong reattachment occurs every other cycle and thus these two cases have a periodicity of two cycles. For example, in Fig. 10 ($\alpha = 4^\circ$), no reattachment of the shear layer is seen at point 3. However, one vortex shedding cycle later at point 7, the upper shear layer clearly reattaches onto the side face and the vortex is formed closer to the rear face of the cylinder. This cyclic pattern repeats itself. Similar events are observed at $\alpha = 6^\circ$ (Fig. 11).

Since at Re = 1000, the upper shear layer interacts with the top rear corner at $\alpha = 2^\circ$, 4° and 6°, it would be reasonable to ask whether there are any finer differences between those three cases. It turns out that the answer is "yes" and the differences can be detected by comparing the surface pressure distributions. In Fig. 12, the time averaged surface pressure distribution for $\alpha = 2^\circ$ and 4° are shown, while in Fig. 13, the time averaged surface pressure distribution for $\alpha = 4^\circ$ and 6° are shown. However, because of the $3T$ periodic nature of the flow at $\alpha = 2^\circ$ and the $2T$ periodic nature of the flow at $\alpha = 4^\circ$ and 6°, different types of time averaged pressure distributions corresponding to the strong reattaching, weak reattaching and nonreattaching cycles are plotted. Altogether five curves are shown in Fig. 12, three for $\alpha = 2^\circ$ and two for $\alpha = 4^\circ$ and 4 curves are shown in Fig. 13, two for $\alpha = 4^\circ$ and two for $\alpha = 6^\circ$.

The reattaching cycle at $\alpha = 4^\circ$ (♦) shows a distinct pressure recovery near the rear corner at side 2 while the nonreattaching cycle (+) shows only a more gradual one. As discussed in Lee (1975), a distinct surface pressure recovery is a strong indication of shear layer reattachment to the side face of the square cylinder. Comparing these pressure plots at $\alpha = 4^\circ$ with those at $\alpha = 2^\circ$, it is noted that the reattaching cycle for $\alpha = 2^\circ$ (○) shows a pressure recovery that is still distinct but slightly less than that at $\alpha = 4^\circ$ (♦). As for the nonreattaching (▲) and weak reattaching (□) cycles at $\alpha = 2^\circ$, they are similar to the nonreattaching case at $\alpha = 4^\circ$. A similar comparison among the pressure plots between $\alpha = 4^\circ$ and 6° in Fig. 13 also reveals that the pressure recovery at 6° for the reattaching cycle (○) is distinct but less than the reattaching cycle at 4° (♦). The conclusion thus reached at this point is that a strong shear layer reattachment (with distinct surface pressure recovery) exists at $\alpha = 4^\circ$ on every other cycle, while relatively weaker reattachments occur at $\alpha = 2^\circ$ and 6°.

However, the above still does not provide an answer as to why an inflection point occurs in the C_y versus α relation at Re = 1000, $\alpha = 4^\circ$. A possible explanation involves the behaviour of the time-averaged trajectory of the shear layers relative to the side faces at different angles of attack. At low angles of attack, the time-averaged trajectories of the two shear layers remain relatively constant. The influence of the rear corner has not been felt by the shear layers even as α varies. As a result, side 2 moves closer to the upper separated shear layer and side 4 moves away from the lower separated shear layer with increasing α. This results in a lower pressure (more suction) on side 2 and a higher pressure (less suction) on side 4. Hence the resultant side force C_y increases over this range of low α.

As α increases further, the rear corner of side 2 is rotated towards the oncoming flow and its presence is detected by the upper shear layer. During the reattachment of the upper shear layer, the rear corner prematurely interrupts the supply of vorticity to the upper primary vortex, resulting in the formation of a weaker vortex. On the contrary, a stronger vortex will be formed when the upper shear layer does not reattach and more circulation can be fed into the primary vortex. Such alternating strength of the upper vortex also affects the location of the lower primary vortex with respect to the wake centre-line. It can be argued here that a stronger upper vortex (which corresponds to a nonreattaching cycle) draws the lower vortex closer to the wake centre-line than a weaker upper vortex. When the lower vortex is drawn nearer to the wake centre-line, the lower separated shear layer is closer to the lower side face (side 4) of the square cylinder, resulting in larger suction on the latter. This is clearly seen in the pressure distribution plots of Figs. 12 and 13 during the nonreattaching cycle for $\alpha = 4^\circ$ (+), along side 4. The pressure distribution on that side at $\alpha = 4^\circ$ during the nonreattaching cycle is one of the most negative, indicating that in that cycle the lower shear layer is close to side 4. On the other hand, a weaker upper vortex (which corresponds to a reattaching cycle) will result in higher (less negative) pressure on side 4 (♦). The discussion given above illustrates that a relatively strong coupling between the primary vortices exists at $\alpha = 4^\circ$ and such strong interactions between the primary vortices causes larger fluctuations in the C_y. From the surface pressure distribution plots, it can be verified that the (cycle averaged) C_y is

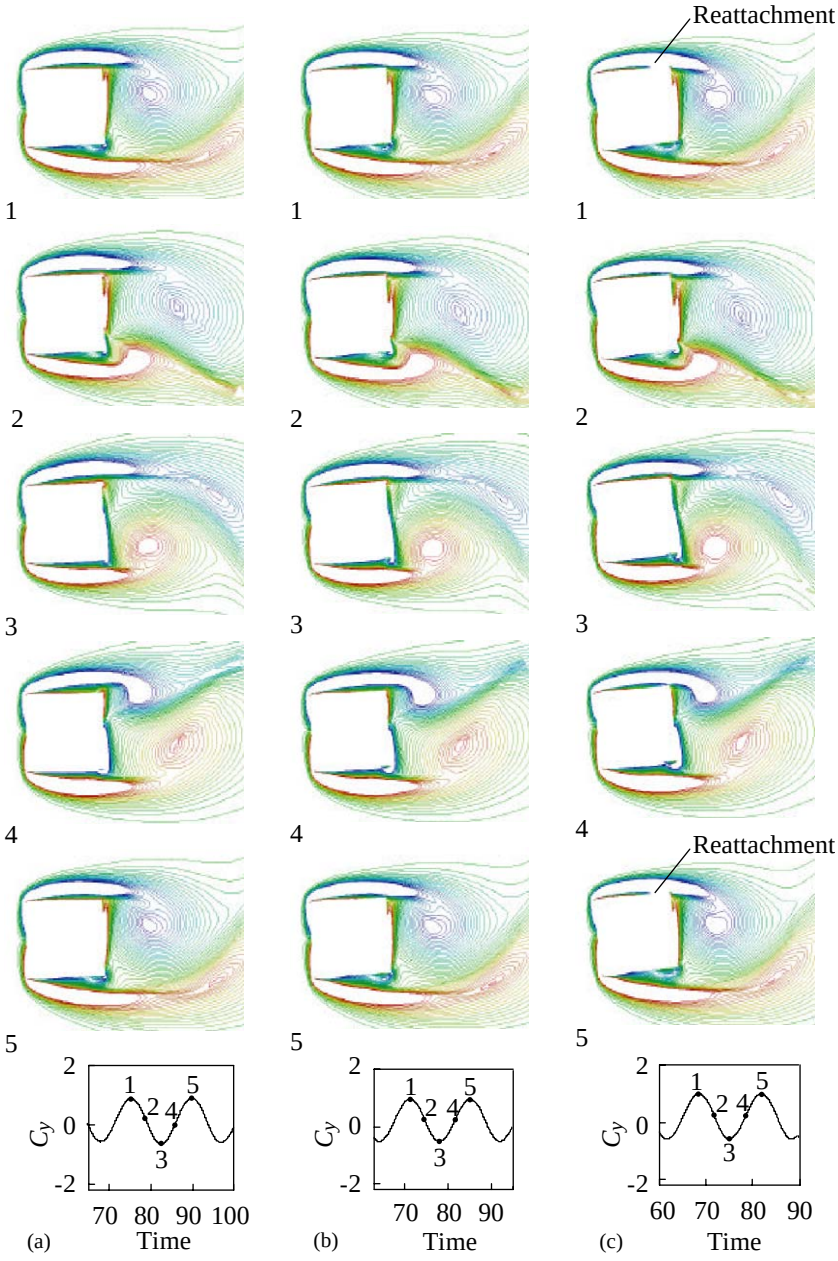

Fig. 8. C_y versus time and the corresponding vorticity contour for Re = 250 at (a) $\alpha = 2^\circ$, (b) $\alpha = 4^\circ$, and (c) $\alpha = 6^\circ$.

positive during the reattaching cycle and negative during the nonreattaching cycle at $\alpha = 4^\circ$. Such fluctuations distort the increasing trend of the average C_y with α and this results in the inflection point that is present in the C_y versus α relation.

As the angle of attack is increased further, this strong coupling between the primary vortices diminishes because of the increased wake width. The distance between the mean trajectory of the upper shear layer and side 2 is decreased while the distance between the mean trajectory of the lower shear layer and side 4 is increased. This causes a further increase in the resultant C_y seen in the C_y versus α relation.

In the next section, the results of an experimental dye flow visualization are described and carried out to verify the numerical results.

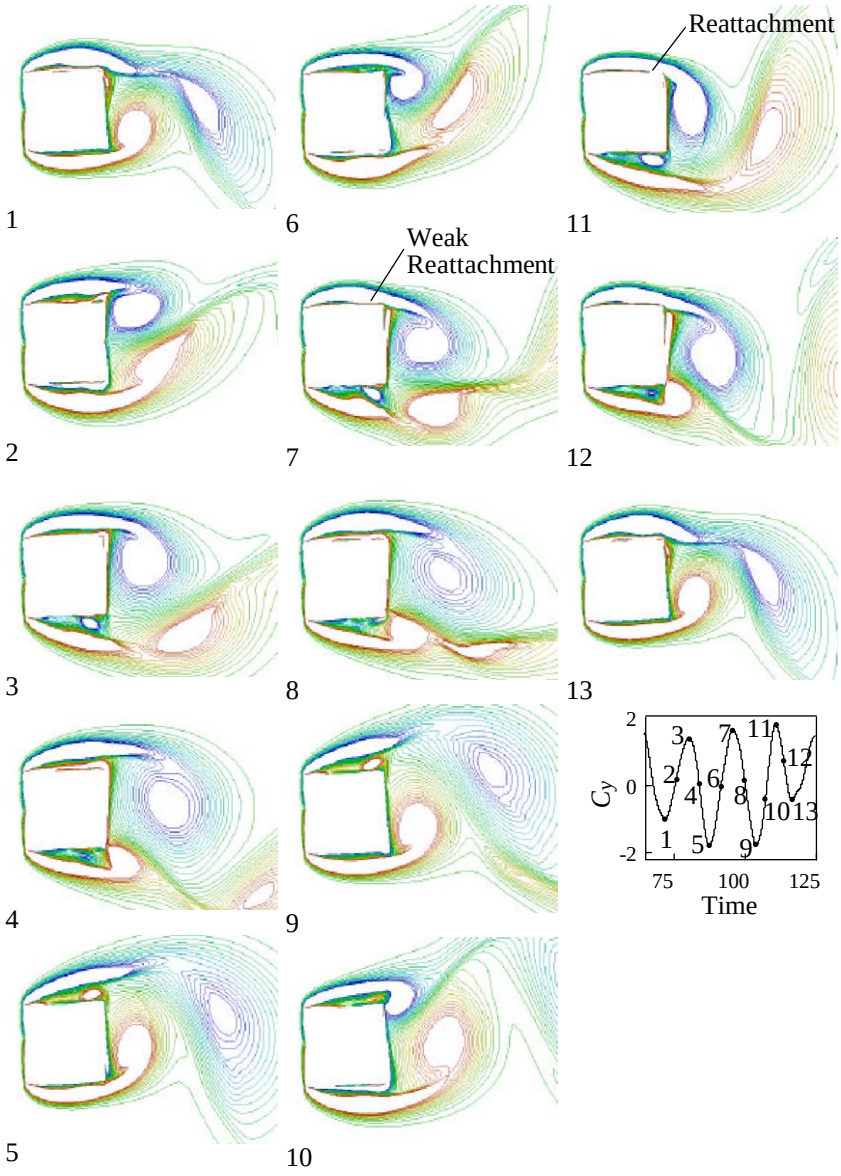

Fig. 9. C_y versus time and the corresponding vorticity contour for Re = 1000, $\alpha = 2^\circ$.

4. Experimental dye visualization

Experimental dye flow visualization was conducted in a water tunnel facility. The main objective in carrying out the flow visualization work is to investigate the existence of the intermittent shear layer reattachment. The experiment was carried out in a recirculating water tunnel, with a working section of 1.83 m (L) × 0.45 m (W) × 0.45 m (D). Two square cylinder models were fabricated from aluminium, one measuring 9.4 mm in side length and the other 18.8 mm. The models were mounted vertically in the water tunnel and circular end plates with chamfered edges were used to minimize the end effects of the model. At the mid-span of the cylinder, dye ports were situated at the front face, near the leading edge of the square cylinder. Coloured dye was released through these ports during the experiment. A video camera was mounted vertically above the square model and images of the vortex shedding process were taken in the $x - y$ (cross-sectional) plane of the model as defined in Fig. 2. The Reynolds numbers investigated were 250 and 1000 and the angles of incidence were 2°, 4° and 6°.

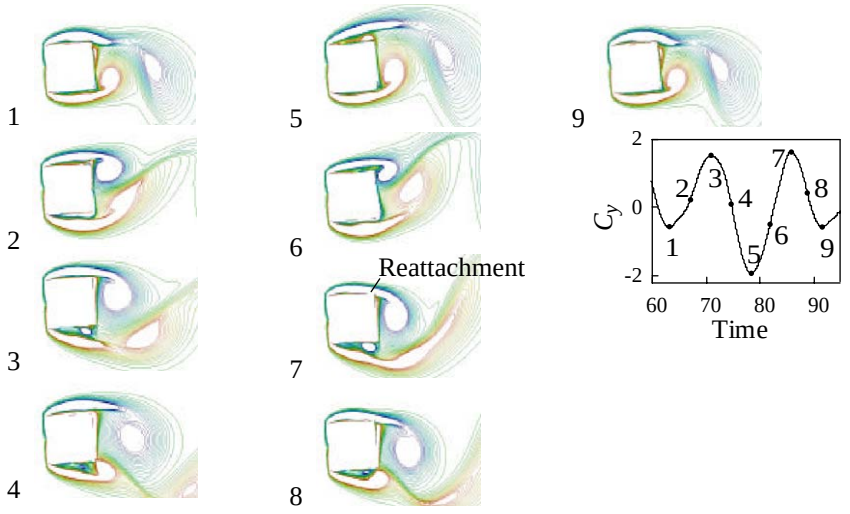

Fig. 10. C_y versus time and the corresponding vorticity contour for Re = 1000, $\alpha = 4°$.

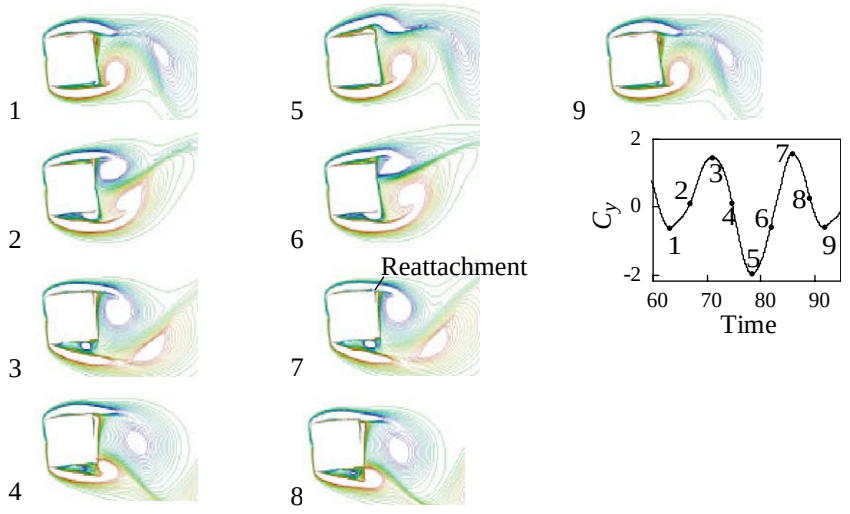

Fig. 11. C_y versus time and the corresponding vorticity contour for Re = 1000, $\alpha = 6°$.

The C_y versus α plot for the case of Re = 250 does not show a point of inflection in the numerical calculation. This is due to the absence of intermittent reattachment of the upper shear layer according to numerical flow visualization. The dye flow visualization results further confirm that there is no intermittent flow reattachment and a more stable wake is present. In Fig. 14, the experimental flow visualization for $\alpha = 2°$, 4° and 6° are shown. For each angle of incidence, a sequence of pictures, which represent one shedding cycle, are shown. These pictures show that the top shear layer does not reattach on to the upper surface of the square cylinder when the angle of incidence increases from 2° to 4°. In this range of angle of incidence, the C_y versus α curve (see Fig. 6a) for Re = 250 increases smoothly and monotonically and it does not show a point of inflection. In Fig. 6a, C_y reaches a maximum point at $\alpha = 5°$, after which it decreases with further increase in α. This decrease is due to the continued reattachment of the upper shear layer onto the top side face of the square cylinder. The experimental flow visualization at $\alpha = 6°$ for Re = 250 shows that reattachment of shear layer occurs at this angle of incidence This is shown in Fig. 14c.

Flow visualization was then repeated at Re = 1000 to investigate the existence of the intermittent reattachment of the upper shear layer. To complement the computed results, the angle of attack investigated were $\alpha = 2°$, 4° and 6°. The readers are reminded at this stage that from the present computational results, a point of inflection in the C_y versus α

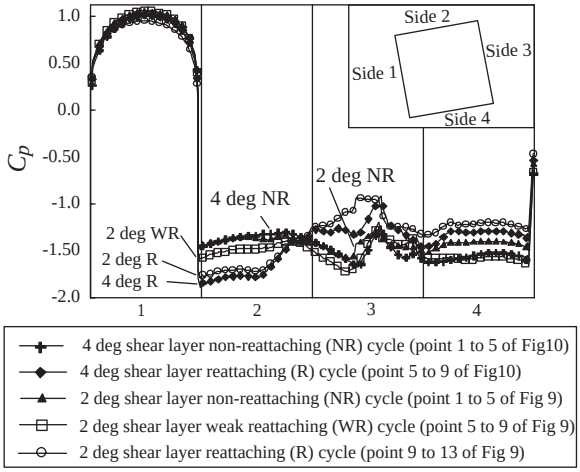

Fig. 12. Time averaged surface pressure distributions for different shedding cycles at Re = 1000, $\alpha = 2^\circ$ and 4°.

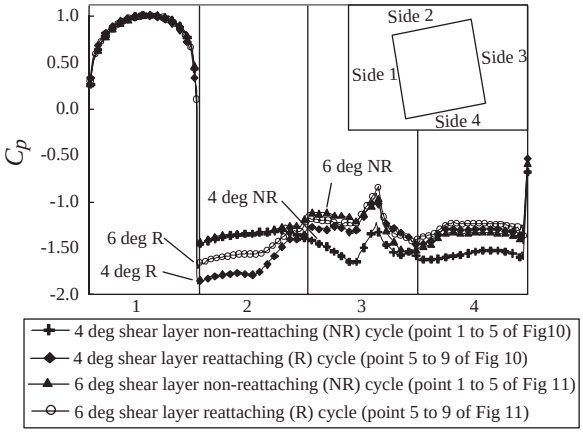

Fig. 13. Time averaged surface pressure distributions for different shedding cycles at Re = 1000, $\alpha = 4^\circ$ and 6° (note that the $\alpha = 4^\circ$ data are identical to those shown in Fig. 12, and are repeated for comparison purposes).

curve was noted to occur at an angle of incidence centred at around 4° (Fig. 6b), and the prime cause was found to be the intermittent and strong reattachment of the upper shear layer onto the side face of the square cylinder. From the flow visualization, intermittent reattachment of the top shear layer was observed at $\alpha = 4^\circ$ and the wake was found to be less stable. Fig. 15a shows a nonreattaching shedding cycle, while Fig. 15b shows a reattaching shedding cycle. When the shear layer reattaches onto the side face of the square cylinder, an enclosed separation bubble is formed and the rear corner of the cylinder stops the further supply of vorticity to the growing vortex. The upper primary vortex was seen to form near the rear face of the cylinder. For the nonreattaching cycle, the primary vortex was noted to form further downstream and the rear corner does not appear to interact with the upper shear layer.

Comparisons between the numerical and experimental dye visualization results are shown side by side in Figs. 16 and 17. In Fig. 16, a reattached upper shear layer is shown, while in Fig. 17, no reattachment of the shear layer is seen. The agreement between the computed and flow visualization results is found to be quite good.

When α is at 2° or 6°, animated CFD visualization results show that the upper shear layer was also seen to interact intermittently with the rear corner. Such interactions consist mainly of relatively weak reattaching cycles and nonreattaching cycles. The present dye visualization supports the CFD findings. At Re = 1000 and $\alpha = 2^\circ$, a weak interaction of the upper shear layer with the rear corner is seen (Fig. 18) and at $\alpha = 6^\circ$, the upper shear layer is also seen to interact with the upper rear corner (Fig. 19). In both cases, the upper primary vortex forms further downstream than the reattaching case at $\alpha = 4^\circ$, indicating a weak cut-off of vorticity by the rear corner.

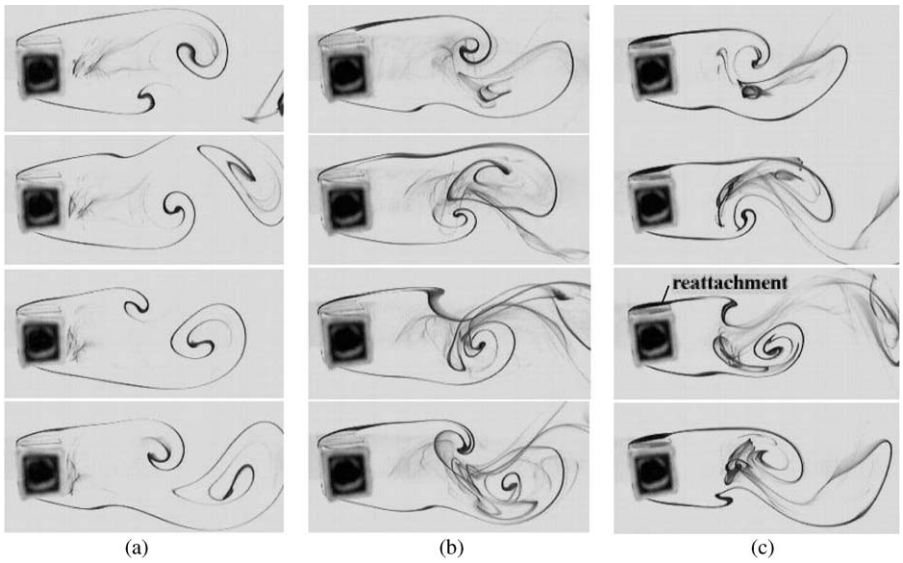

Fig. 14. Dye flow visualization for square cylinder at Re = 250 and (a) $\alpha = 2^\circ$, (b) $\alpha = 4^\circ$, and (c) $\alpha = 6^\circ$. Upper shear layer reattachment is detected at $\alpha = 6^\circ$ but not at $\alpha = 2^\circ$ and 4°.

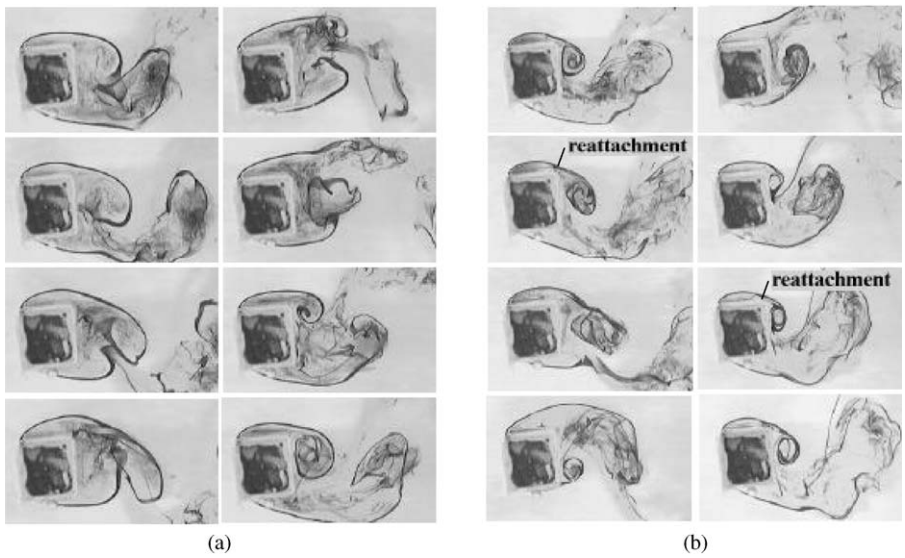

Fig. 15. Dye flow visualization for two typical vortex shedding cycles at Re = 1000, $\alpha = 4^\circ$, showing a cycle with (a) shear layer reattachment absent and (b) shear layer reattachment occurring (vortex shedding sequence runs downwards from the top left picture and ends in the bottom right picture of each series).

Although in general the flow visualization results support the CFD findings, there are also some discrepancies between them. In particular, while the numerical results at Re = 1000 and at $\alpha = 4^\circ$ predict that the intermittent reattachment occurs very regularly in an alternate shedding cycle manner, from the experimental flow visualization, it was noted that the vortex shedding process consists of a few consecutive reattaching cycles followed by a few nonreattaching cycles. This discrepancy can be explained by the fact that the results obtained computationally were modelled under ideal conditions, whereas in the experiments, the conditions are usually far from ideal. For example, based on the findings reviewed in Williamson (1996), flow structures at Re = 250 and 1000 are three-dimensional even when the cylinder end effects are isolated. However, in the present computation three dimensionality in the vortex

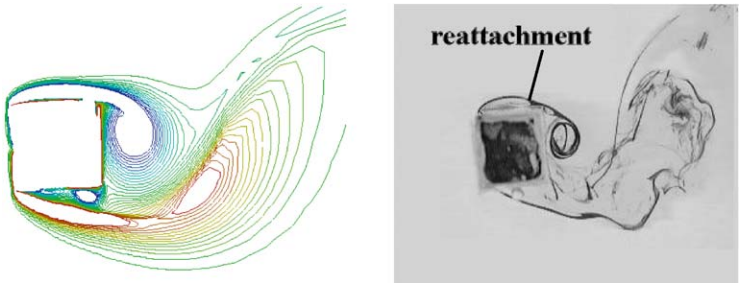

Fig. 16. Comparison between numerical and experimental flow visualization at Re = 1000, $\alpha = 4^\circ$. A reattached upper shear layer is seen.

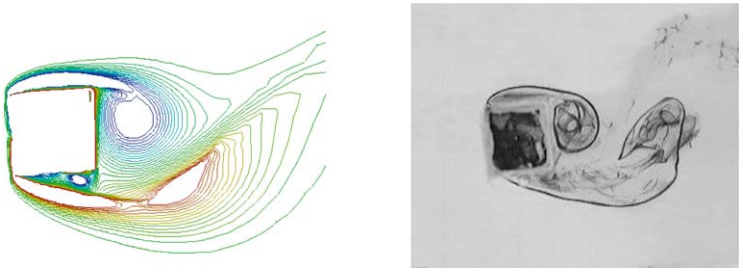

Fig. 17. Comparison between numerical and experimental flow visualization at Re = 1000, $\alpha = 4^\circ$. No reattachment of the upper shear layer is seen.

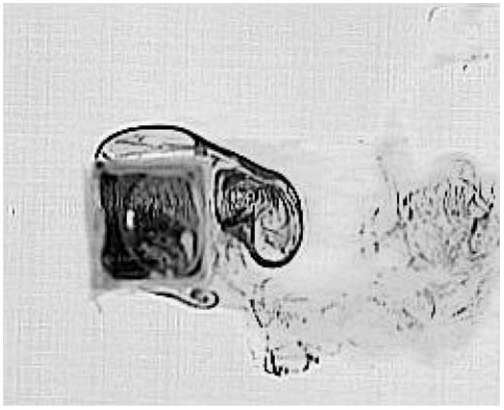

Fig. 18. A weak reattachment of the upper shear layer at Re = 1000, $\alpha = 2^\circ$.

shedding process is not accounted for. Another factor that can contribute to the differences in computational and experimental results is the presence of free stream turbulence. In Vickery (1966), Barriga et al. (1975), Lee (1975), Robertson et al. (1977), and Obasaju (1983), they noted that increasing the level of turbulence intensity encourages the reattachment of shear layer onto the side face of a square cylinder.

Finally, it should be mentioned that the vortex formation region shown in the dye flow visualization for Re = 250 appears to be larger than that obtained from numerical simulation; whereas at Re = 1000 the experimental and numerical visualizations appear to be in better agreement. One possible explanation for the above observation is that, in order to achieve the two different Re of 250 and 1000, both the model size and the flow speed of the former were half of the latter. With a slower flow speed, the dye takes a longer time to get entrained into the near wake, resulting in the apparently larger vortex formation region. However, in spite of the above-mentioned difference between the experimental and computational results, the flow visualization results still clearly support the important features observed in the computation.

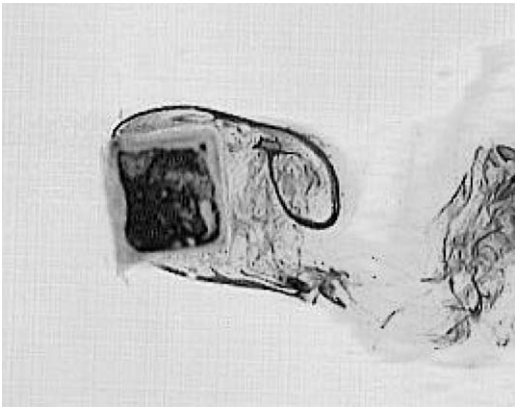

Fig. 19. A weak reattachment of the upper shear layer at Re = 1000, $\alpha = 6^\circ$.

5. Conclusion

In the present paper, a hybrid vortex method was used to simulate the flow over a stationary square cylinder at incidence and at Reynolds number of 250 and 1000. The computed results reveal that the C_y versus α curve at Re = 250 does not contain a point of inflection, but an inflection point exists in the case of Re = 1000 at $\alpha = 4^\circ$. Further work revealed that a strong but intermittent shear layer reattachment occurs at Re = 1000 and $\alpha = 4^\circ$, but not at Re = 250. It is believed that the intermittent reattachment results in large fluctuation in C_y, and eventually a point of inflection in the C_y versus α relation. Computed results also show that although at Re = 1000 the shear layer does interact with the rear corner at $\alpha = 2^\circ$ and 6°, the shear layer reattachment was weaker than that at $\alpha = 4^\circ$. Using quasi-steady theory as outlined in Pakinson and Smith (1964), the authors were able to demonstrate that the point of inflection in the C_y versus α relation directly results in the hysteresis seen in the $\bar{Y}$ versus U relation. Thus, it can be concluded that the existence of intermittent shear layer reattachment (and hence an inflection point in the C_y versus α relation) leads to the existence of a hysteresis region in the amplitude–velocity characteristic for a galloping square cylinder.

References

Barriga, A.R., Crowe, C.T., Roberson, J.A., 1975. Pressure distribution on a square cylinder at a small angle of attack in a turbulent cross flow. Proceedings of the 4th International Conference on Wind Effects on Building and Structures. Heathrow, England, Cambridge University Press, pp. 89–93.

Bearman, P.W., Luo, S.C., 1988. Investigation of the aerodynamic instability by forced oscillation. Journal of Fluid and Structures 2, 161–176.

Bearman, P.W., Gratshore, I.S., Maull D, J., Parkinson, G.V., 1987. Experiments on flow induced vibration of a square-section cylinder. Journal of Fluids and Structures 1, 19–34.

Blevins, R.D., 1990. Flow Induced Vibrations, 2nd Edition. Van Nostrand Reinhold, New York.

Cheng, M., Chew, Y.T., Luo, S.C., 1997. A hybrid vortex method for flows over a bluff body. International Journal for Numerical Methods in Fluids 24, 253–274.

Davis, R.W., Moore, E.F., 1982. A numerical study of vortex shedding from rectangles. Journal of Fluid Mechanics 116, 475–506.

Lee, B.E., 1975. The effects of turbulence on the surface pressure field of a square cylinder. Journal of Fluid Mechanics 69, 263–282.

Luo, S.C., Yazdani, M.G., Chew, Y.T., Lee, T.S., 1994. Effects of incidence and afterbody shape on flow past bluff cylinders. Journal of Wind and Industrial Aerodynamics 53, 375–399.

Norberg, C., 1993. Flow around rectangular cylinders-pressure and wake frequencies. Journal of Wind Engineering and Industrial Aerodynamics 49, 187–196.

Obasaju, E.D., 1983. An investigation of the effects of incidence on the flow around a square section cylinder. Aeronautical Quarterly 34, 243–259.

Parkinson, G.V., Brooks, N.P.H., 1961. On the aeroelastic instability of bluff cylinders. Journal of Applied Mechanics 28, 252–258.

Parkinson, G.V., Smith, J.D., 1964. The square cylinder as an aeroelastic non-linear oscillator. Quarterly Journal of Mechanics and Applied Mathematics 17, 225–239.

Parkinson, G.V., Wawzonak, M.A., 1981. Some consideration of combined effects of galloping and vortex resonance. Journal of Wind and Industrial Aerodynamics 8, 135–143.

Robertson, J.M., Wedding, J.B., Peterka, J.A., Cermak, J.E., 1977. Wall pressures of separation—reattachment flow on a square prism in uniform flow. Journal of Industrial Aerodynamics 2, 345–360.

Shiau, Y.H., Peng, Y.F., Hwang, R.R., Hu, C.K., 1999. Multistabilty and symmetry breaking in the two-dimensional flow around a square cylinder. Physical Review E 60 (5), 6188–6191.

Sohankar, A., Norberg, C., Davidson, L., 1999. Simulation of three-dimensional flow around a square cylinder at moderate Reynolds numbers. Physics of Fluids 11, 288–306.

Vickery, B.J., 1966. Fluctuating lift and drag on a long cylinder of square cross-section in a smooth and in a turbulent flow. Journal of Fluid Mechanics 25, 481–494.

Williamson, C.H.K., 1996. Vortex dynamics in Cylinder Wakes. Annual Review of Fluid Mechanics 28, 477–539.